Journal of Materials Chemistry A

Structural evolution, electrochemical kinetic properties, and stability of A-site doped perovskite Sr1-xYbxCoO3-□

Journal:	*Journal of Materials Chemistry A*
Manuscript ID	TA-ART-03-2020-003476.R1
Article Type:	Paper
Date Submitted by the Author:	29-Apr-2020
Complete List of Authors:	Yang, Chunyang; University of South Carolina, Mechanical Engineering Gan, Yun; University of South Carolina, Mechanical Engineering Lee, Myongjin; University of South Carolina ren, Chunlei; University of South Carolina, Mechanical Engineering Brinkman, Kyle; Clemson University, Materials Science and Engineering Green, Robert; NASA Glenn Research Center, Xue, Xingjian; University of South Carolina, Mechanical Engineering

Structural evolution, electrochemical kinetic properties, and stability of A-site doped perovskite $Sr_{1-x}Yb_xCoO_{3-\delta}$

Chunyang Yang[a], Yun Gan[a], Myongjin Lee[a], Chunlei Ren[a], Kyle S. Brinkman[b], Robert D. Green[c], and Xingjian Xue[a,*]

[a] Department of Mechanical Engineering, University of South Carolina, Columbia, SC 29208, USA.

[b] Materials Science and Engineering, Clemson University, Clemson, SC 29634, USA.

[c] NASA Glenn Research Center, Cleveland, OH 44135, USA

*Corresponding Author. Tel:1-803-576-5598; Fax: 1-803-777-0106; Email: Xue@cec.sc.edu (X. Xue)

Abstract:

Mixed ionic and electronic conducting (MIEC) perovskite $SrCoO_{3-\delta}$ is a widely studied (electro) catalyst for oxygen reduction reactions (ORRs) and possesses different crystal structures at different temperatures. These temperature dependent phase transitions significantly impact the ordering of oxygen vacancies and electrochemical kinetic properties as well as the reliability of related devices. Some of the crystal structures formed, e.g., hexagonal phases, turn out to be almost impermeable to oxygen gas. Therefore, it is important to stabilize the crystal structure of $SrCoO_{3-\delta}$ that favors ORRs over a wide temperature range. Herein, the partial substitution of the A-site Sr with Yb is systematically studied, including synthesis, characterization and analysis of structural evolution, electrochemical kinetic properties, thermal stability, and stability in CO_2-containing atmosphere. The results indicate that $Sr_{0.90}Yb_{0.10}CoO_{3-\delta}$ is able to stabilize the tetragonal crystal structures with less ordered oxygen vacancies and leads to polarization resistances of 0.051, 0.115 and 0.272 Ω cm^2 at 750, 700 and 650 ^{o}C, respectively, on symmetrical cells. $Sr_{0.90}Yb_{0.10}CoO_{3-\delta}$ demonstrates very stable surface oxygen vacancy distribution and electronic structure near oxygen vacancies but dissociation of adsorbed oxygen molecule into atom oxygen process is affected by surface Sr segregation, and polarization resistance degradation is mainly induced by

surface Sr segregation. Furthermore, $Sr_{0.90}Yb_{0.10}CoO_{3-\delta}$ exhibits excellent thermal stability as well as excellent recovery stability and improved polarization performance after a few pure air/CO_2-containing air treatment cycles at 700 ^oC. However, a hysteresis behavior of polarization performance is observed at 650 ^oC during gas cycling treatment, which may cause long-term degradation of $Sr_{0.90}Yb_{0.10}CoO_{3-\delta}$ electrode. The different polarization behaviors during gas cycling treatment are induced by different sensitivities of the formed surface strontium carbonate and chemisorbed surface oxo-carbonaceous species to different operating temperatures.

I. Introduction

Solid oxide fuel cells (SOFCs) convert chemical energy in fuels into electrical energy in a highly efficient and environment friendly manner, and have been widely studied.[1] In order to obtain high electrochemical performance, early stage SOFCs are usually operated at high temperatures (above 800 ^oC). This operating temperature may increase system and operating cost, limit material selections, and cause material and microstructure degradation.[2] To overcome these issues, it is suggested that the operating temperature of SOFCs be reduced to intermediate range (600-800 ^oC).[1, 3] Nevertheless, lowering the operating temperature would increase resistance losses of charge transport and surface exchange kinetic processes, especially polarization losses induced by the cathodic electrode process.[4] Thus, it is very important to develop cathode materials suitable for intermediate temperature SOFCs (IT-SOFCs).

Perovskite-type mixed ionic and electronic conducting (MIEC) materials have high flexibility to tune their physical properties such as oxygen vacancies, structural symmetry, lattice free volumes, metal-oxygen bonding energies. These properties are strongly dependent on crystal structure and significantly affect electrochemical kinetic properties and stability of the materials.[5, 6] Strontium cobaltite ($SrCoO_{3-\delta}$) is a typical perovskite MIEC showing high electrical conductivity and electrocatalytic property as a cathode material for SOFCs and has been widely used as a parent compound to derive other high performance MIEC cathodes.[7] Depending on annealing temperature and oxygen partial pressure during synthesis/fabrication

process, $SrCoO_{3-\delta}$ may adopt a variety of crystal structures, e.g., orthorhombic, tetragonal and cubic. For example, $SrCoO_{3-\delta}$ forms an oxygen vacancy-ordered orthorhombic brownmillerite phase below 653 ^{o}C, and will transfer to a 2-H type hexagonal phase between 653 and 920 ^{o}C, eventually changes to a cubic or tetragonal perovskite phase above 920 ^{o}C. However, the high temperature phase will transit reversibly to a hexagonal phase as temperature drops from a high (> 920 ^{o}C) to intermediate temperature range.[8] These phase variations directly affect oxygen vacancy features and the electrochemical properties of $SrCoO_{3-\delta}$. For example, the vacancy ordered state at low temperatures transforms to a disordered state above 900 ^{o}C; the resulting hexagonal phase is almost impermeable to oxygen gas.[9] Interestingly, the high temperature phase of $SrCoO_{3-\delta}$, a cubic phase, demonstrates the best electrochemical kinetic properties among all the phases.[7 10] Therefore, it is important to stabilize the cubic phase of $SrCoO_{3-\delta}$ in a wide temperature range (from high to room temperature) to prevent phase transition reversibly upon temperature decrease.

The Goldschmidt tolerance factor is able to describe the distortion degree of a perovskite structure from the standard cubic one. To form a cubic perovskite structure, the corresponding Goldschmidt tolerance factor should be close to 1. Given ionic radii of $r(Sr^{2+})(XII) = 1.44$ Å, $r(Co^{4+})(VI) = 0.53$ Å, $r(O^{2-})(VI) = 1.40$ Å,[11] the theoretical Goldschmidt tolerance factor of an ideal stoichiometric perovskite $SrCoO_3$ is 1.04. To tune the tolerance factor closer to 1, two doping strategies can be utilized. One is B-site doping using the elements with ionic radius being greater than $r(Co^{4+})(VI)$, such as Nb, Sc, Ti, Sb, Mo and Ta.[12-18] However, a relatively high content of such elements, e.g., up to 20 mol% amount B-site doping, is required in order to stabilize cubic phase. This could deteriorate oxygen reduction reaction properties of the material, which are strongly dependent on valance and spin state of the B-site elements. Another strategy is to dope the element with smaller size than $r(Sr^{2+})(XII)$ on A-site, which is much less studied in the literature. The radii of lanthanides in 12-fold coordinates decrease with an increase in atomic number, e.g., $r(La^{3+})(XII) = 1.36$ Å, $r(Ce^{3+})(XII) = 1.34$ Å, $r(Nd^{3+})(XII) = 1.27$ Å and $r(Sm^{3+})(XII) = 1.24$ Å. Even though exact radius of $Yb^{3+}(XII)$ is not available in the radius chart, it is anticipated that Yb^{3+} in 12-fold coordinates would be smaller than that of Sm^{3+}.[11] This is consistent with those reported in other references, i.e., 1.22[19], 1.07[20] and 1.01[21] Å for Yb^{3+} in 12-fold coordinates. Therefore, a partial substitution of Sr by Yb

on the A-site is expected to be able to tune the tolerance factor closer to 1, potentially stabilizing the cubic perovskite structure of $SrCoO_{3-\delta}$.

It has been recognized that Sr in $SrCoO_{3-\delta}$ can be demixed and segregated onto the surface of bulk cathode, leading to deterioration of electrode performance.[22, 23] Under practical operating conditions, an oxygen/air atmosphere surrounding the SOFCs cathode could contain a small amount of CO_2. When exposed to a CO_2-containing atmosphere, surface Sr could react with CO_2 to form carbonates on the oxide surface, blocking oxygen surface exchange.[24, 25] For instance, polarization resistances of $Ba_{0.5}Sr_{0.5}Co_{0.8}Fe_{0.2}O_{3-\delta}$ and $SrSc_{0.175}Nb_{0.025}Co_{0.8}O_{3-\delta}$ cathode increase about 25 and 35 times, respectively, when exposed to 5% CO_2-containing air for 15 min compared to CO_2-free air at 600 ^oC.[26] After switching back to pure air, polarization resistances still remain over 2 times higher than the original ones due to the formation of surface (Ba, Sr)CO_3 compound.[26] In theory, the average bonding energy (ABE) can be used to evaluate stability of a material in different atmospheres. Taking $Sr_{1-x}Yb_xCoO_{3-\delta}$ as an example, with Co element on the B-site, calculations of Sr-O and Yb-O bonding energy in such ABO_3 perovskites are sufficient for their ABE comparison. Simple calculations indicate that the ABE of Yb-O, -119.45 kJ mol^{-1} is more negative than that of Sr-O, i.e., -83.80 kJ mol^{-1}.[27] Therefore, it is reasonable to expect that partial substitution of Sr on the A-site by Yb may lead to less oxygen loss and better thermal stability at elevated temperatures, and could also improve stability in CO_2 containing atmospheres. In addition, Yb possesses a higher electronegativity value (~1.1) than Sr (1.0)[28], meaning that Yb has a stronger power to attract electrons than Sr. Therefore, partial substitution of Sr with Yb on the A-site can decrease the basicity of the material and thus increase resistance against acidic gases.

In this research, a new series of $Sr_{1-x}Yb_xCoO_{3-\delta}$ (x = 0.05, 0.10 and 0.15) was synthesized and characterized including crystal structure evolution with Yb doping levels, oxygen reduction reaction kinetics and associated rate limiting steps, thermal stability, and stability in CO_2-containing atmosphere at elevated temperatures.

II. Experimental procedure

2.1 Powder synthesis

$Sr_{1-x}Yb_xCoO_{3-\delta}$ (x = 0, 0.05, 0.10 and 0.15, simply denoted as SYbC0, SYbC5, SYbC10 and SYbC15, respectively) powders were synthesized by a combined ethylenediaminetetraacetic acid (EDTA)-citrate acid complexing sol-gel process. Specifically, stoichiometric amounts of $Sr(NO_3)_2$ (Alfa Aesar, 99.0%), Yb_2O_3 (Alfa Aesar, 99.99%) and $Co(NO_3)_2 \cdot 6H_2O$ (Alfa Aesar, 99.999%) were dissolved in diluted nitric acid. After a transparent solution formed under magnetic stirring, citric acid (99.0-102.0%, BDH) and EDTA (99.4-100.6%, BDH) were added into the solution with molar ratio of citric acid:EDTA:metal ions = 1.5:1:1 as complexants. The pH value of the solution was adjusted to about 8 by adding ammonium hydroxide. After being mixed homogenously, the precursor solution was heated in a water bath at 80 ^oC to evaporate excess water until a viscous gel was obtained. An electrical burner was then used to heat the gel until self-burned, forming a bouffant ash. The resulting precursor powder was ground and then calcined at 400 ^oC for 2 h to remove organic residues, and then 1000 ^oC in air for 6 h to form $Sr_{1-x}Yb_xCoO_{3-\delta}$ (denoted as SYbCx) phase, followed by high energy ball milling for 1 h with ethanol as milling medium.

2.2 Symmetrical cell preparation

To characterize the electrochemical performance of synthesized SYbCx materials, symmetrical cells with configuration of SYbCx/$Ce_{0.8}Sm_{0.2}O_{1.9}$/SYbCx were fabricated. $Ce_{0.8}Sm_{0.2}O_{1.9}$ (SDC) electrolyte powder (tape cast grade, Fuel Cell Material, USA) was mixed and ground with a binder of polyvinyl butyral (PVB, 2 wt.%) in ethanol. After completely dried, the powder was uniaxially pressed at around 200 MPa using a stainless steel die to form a disk with a diameter of ~15 mm. Green pellets were then sintered and densified at 1450 ^oC in air for 6 h. Surfaces of densified SDC pellets were polished with sand paper and then cleaned in ethanol in an ultrasonic cleaner. SYbCx cathode powders were mixed with a balanced amount of 6 wt.% ethyl cellulose-terpineol binder to form a cathode ink, which was then screen-printed

onto both sides of each SDC pellet. After drying and aging, the symmetrical cells were sintered at 1050 °C in air for 2 h. Silver paste and wire were attached at either surface of electrodes as current collectors.

2.3 Characterization

X-ray diffraction (XRD, D/MAX-3C) with Cu Kα radiation (λ = 1.5406 Å) was employed to characterize phase purity and crystal structure of powder materials at room temperature. XRD data was collected over a 2θ range from 10-90° with a step size of 0.02°. Rietveld refinements were performed on XRD patterns of SYbC5 and SYbC10, respectively, with GSAS-II/EXPGUI software.[29] Transmission electron microscopy (TEM) measurements were performed on a Hitachi H-9500 TEM with an accelerating voltage of 300 kV. To prepare samples for TEM measurements, nanoparticle samples were diluted in ethanol and sonicated for 30 min to ensure a homogeneous distribution of particles. Two drops of the suspension were deposited onto a carbon stabilized Formvar-coated copper grid and completely dried at room temperature prior to measurement. The microstructure of the prepared samples was characterized with scanning electron microscope (SEM, Zeiss Ultra Plus FESEM, Germany).

Electrochemical impedance spectroscopy (EIS) of symmetrical cells with SYbC5 and SYbC10 as electrode materials was measured using a Zahner IM6E electrochemical workstation under open circuit voltage in the frequency range from 10^6 to 0.1 Hz with a voltage perturbation of 10 mV. To further investigate the kinetics of oxygen reduction reactions of cathode material, polarization resistances at different oxygen partial pressure ($p(O_2)$) and different temperatures were measured. Various $p(O_2)$ were obtained by adjusting the flow rate ratios of oxygen *vs.* nitrogen, controlled by flow meters (APEX). Oxygen and nitrogen were supplied to a three-way valve through two individual lines and mixed. The mixed oxygen/nitrogen gas then flowed into a surge flask before entering the alumina test chamber.

The stability of the synthesized material was characterized, including crystal structure stability and long-term stability as cathode material as well as stability in CO_2-containing atmosphere. In particular, to examine thermal stability, powders were annealed at 700 °C in air for 250 h, followed by XRD

characterization. Long term stability of SYbC10 as cathode material was characterized at 700 °C in air for ~ 300 h, during which polarization resistance of symmetrical cell SYbC10/SDC/SYbC10 was measured periodically. CO_2 tolerance and recovery capability of SYbC10 as cathode material were also characterized using symmetrical cell at 700 and 650 °C respectively. The atmosphere surrounding symmetrical cell was switched periodically between pure air and 5% CO_2-air. The polarization resistance of the symmetrical cell was measured every half hour.

III. Results and discussion

3.1 Crystal structure characterization and analysis of as-prepared $Sr_{1-x}Yb_xCoO_{3-\delta}$ powders

The synthesis of a perovskite material usually starts from a precursor powder preparation, followed by calcination at elevated temperatures to form a desired crystal phase. After cooling down, the formed phase at elevated temperatures is remained at room temperature. Unfortunately, undoped strontium cobalt oxide loses lattice oxygen at elevated temperature, forming $Sr_2Co_2O_5$ as described by reaction (1). During the cooling down process, $Sr_2Co_2O_5$ absorbs oxygen from air, forming $Sr_6Co_5O_{15}$ and Co_3O_4 as expressed by reaction (2).[30-33]

$$2SrCoO_{3-\delta} \leftrightarrow Sr_2Co_2O_5 + \frac{(1-2\delta)}{2}O_2 \quad (1)$$

$$3Sr_2Co_2O_5 + \frac{2}{3}O_2 \leftrightarrow Sr_6Co_5O_{15} + \frac{1}{3}Co_3O_4 \quad (2)$$

As shown in Fig. 1, XRD patterns of our synthesized undoped $SrCoO_{3-\delta}$ does indeed consist of $Sr_6Co_5O_{15}$ and Co_3O_4, confirming that it is very difficult to synthesize a pure $SrCoO_{3-\delta}$ phase. Interestingly, upon substitution of Sr by Yb, the material phase is stabilized and exhibits a higher symmetrical perovskite phase. It is easy to see that SYbC5 and SYbC10 powders are well crystalized to a single phase respectively. With increasing Yb doping level to 15 mol%, secondary phase peaks appear in the SYbC15 XRD patterns (Fig. 1), implying that a 10 mol% doping level seems to be the upper-limit for Yb solubility on the A-site of $SrCoO_{3-\delta}$. Using the basis of cubic structure (JCPDS 38-1148), indices of diffraction peaks of SYbC5 and SYbC10 are marked in Fig. 1, indicating that main features of the XRD patterns could be explained by

cubic phase with the perovskite structure. Accordingly, these materials exhibit a higher symmetrical structure of perovskite phase upon A-site partial substitution of Sr by Yb.

Fig. 2a shows magnified XRD patterns of SYbC5 and SYbC10 in the range of 2θ = 38-56°. One can see that some small peaks appear at 42° and 48.5° in diffraction patterns. The magnified XRD patterns around $(200)_c$, $(211)_c$, $(220)_c$ in Fig. 2b demonstrate increasingly obvious peak splitting of the XRD patterns. It is not straightforward to interpret either additionally appeared small peaks or peak splitting based on the understanding of cubic crystal structure. The peak variations could be related to the distribution of oxygen vacancies in the crystal structure, for instance, oxygen vacancies in perovskite phase are not disordered completely and vacancy ordering can appear locally.[34] In fact, upon oxygen vacancy ordering, tetragonal superstructures (*I4/mmm*) can occur in Co-based perovskites, and has following relationship with the corresponding unit cell:

$$a_t \times a_t \times c_t \approx 2a_c \times 2a_c \times 4a_c \quad (3)$$

where a_t and c_t are lattice parameters of the tetragonal structure, while a_c is one of the corresponding primitive cubic unit cell.[35, 36] The two additional small peaks at 42° and 48.5° could originate from the supercell formed upon vacancy ordering, which can also explain the splitting of the peaks.[34] Thus, more than likely, the structures of SYbC5 and SYbC10 are tetragonal with oxygen ordering vacancies instead of cubic perovskite with disordered vacancies. With increasing Yb content from 5 to 10 mol%, two small peaks at 42° and 48.5° become less pronounced, indicating dissolution of the oxygen-ordered superlattice into an oxygen-disordered primitive cubic structure. Seemingly, a structural transition takes place from tetragonal towards cubic. In the meantime, the peaks shift to higher angles as shown in Fig. 2, indicating that such a structural transition is accompanied by lattice shrink.

To further understand XRD data and examine the above analysis, Rietveld refinement was performed on these experimental XRD patterns of SYbC5 and SYbC10 by using the GSAS-II program, where the tetragonal structure with *I4/mmm* space group was used as an initial model. Fig. 3a and 3b show the refinement results of XRD patterns for SYbC5 and SYbC10, respectively. Table 1 lists the details of fitting

and structure parameters. A reasonable low weighted profile R-factor (R_{wp}), integrated intensity R-factor ($R_F{}^2$) and goodness of fit (χ^2) are achieved when the tetragonal *I4/mmm* space group is used to fit the experimental XRD data. And a good agreement was achieved between XRD profile and the fitting results as graphically shown in Fig. 3, which ensures a good quality for Rietveld refinement. It can also be observed that partial substitution of Sr by Yb leads to smaller lattice and cell volumes, which is consistent with the XRD peak shifting in Fig. 2. With increasing Yb-doping levels from 5 to 10 mol%, the corresponding $c_t/2a_t$ ratio gradually closes to 1, leading to a structural transition tendency towards a cubic lattice. This result is also consistent with the above analysis of crystal structure evolution. Schematics of crystal structures of SYbC0 and SYbC10 are shown in Fig. S1 (supplementary information).

A transmission electron microscope (TEM) was employed to further characterize crystal structures of SYbC5 and SYbC10. Fig. 4a and 4b show micro-morphology of SYbC5 and SYbC10 powders, respectively. More TEM images of SYbC10 powders are also provided in Fig. S2. It can be seen that the powders consist of both large particles and small spherical particles. The small spherical particles with a diameter of ~2-3 nm can be observed (see dashed circle marks in Fig 4 and Fig. S2). Additionally, some larger particles are formed with the aggregation of small spherical particles (Fig. S2). High-resolution TEM images in selected regions of SYbC5 and SYbC10 exhibit well-defined crystalline fringes as shown in Fig. 4c and 4d respectively. Interplanar distances of 0.283 nm and 0.258 nm were obtained from the fringe measurements for SYbC5 and SYbC10, respectively, which is related to the $(220)_t$ or $(110)_c$ lattice plane as shown in Fig. S3. Although interplanar distances obtained from these TEM images show a little bit difference from the above Rietveld refinement result due to measurement and fitting errors, variation tendency of lattice parameters is consistent with each other. All of these results suggest that partial substitution of Sr with 5 and 10 mol% Yb on A-site exhibits an evolution of the corresponding lattice structure and is able to stabilize high temperature phase of $SrCoO_{3-\delta}$ to room temperature.

3.2 Structural stability of synthesized powders after thermal treatment

SOFCs operate at elevated temperatures and require long-term stability of the involved materials, in particular, the cathode materials. The purpose of the partial substitution of Sr with Yb in $SrCoO_{3-\delta}$ mentioned above is to stabilize the high temperature crystal structure down to room temperature, so that crystal structure stability can be obtained in a wide operating temperature range. In this section, the thermal stability of the synthesized powders of SYbC5 and SYbC10 is evaluated. In particular, the as-prepared SYbC5 and SYbC10 powders were annealed at 700 °C in air for 250 h. The XRD patterns of the powders before and after annealing treatment were obtained. As shown in Fig. 5, the materials maintained the same crystal structures before and after annealing treatment, indicating that both SYbC5 and SYbC10 powders are thermally stable at 700 °C in air.

3.3 Electrochemical performance and stability of SYbC5 and SYbC10 as electrode materials

3.3.1 Yb doping level effect on polarization resistances of SYbC5 and SYbC10 cathodes

To evaluate Yb dopant effect on electrochemical performance of SYbC5 and SYbC10, the polarization resistance (R_p) was measured on symmetrical cells using EIS under open circuit voltage conditions in the temperature range of 600-750 °C. SEM images (Fig. S4) show that SYbC5 and SYbC10 cathodes demonstrate intimate contact with SDC electrolyte and have sufficient porosity; the sintered particles also show good inter-connectivity throughout the cathode.

Fig. 6 shows typical EIS of SYbC5 and SYbC10 electrodes measured at 700 °C in air. Spectra fitting results are shown in the same figure using an equivalent circuit with the configuration of $L - R_o - (R_hQ_h) - (R_lQ_l)$ (inset in Fig. 6a). Here, L denotes inductance of the circuit, R_o represents ohmic resistance induced by electrolyte and electrode backbone as well as current collecting wires. R_i and Q_i are the resistance and constant phase capacitance of high (h) and low (l) frequency processes, respectively. The fitting results of R_h and R_l are corrected by electrode area and divided by two due to the symmetrical configuration of the cell. The polarization resistance of electrode R_p is then obtained by adding R_h and R_l together. The Bode plot in Fig. 6b shows the frequency response of the imaginary part of the impedance

spectra, indicating that the improved performance of SYbC10 electrode is mainly associated with low frequency processes. Arrhenius plots of R_p of SYbC5 and SYbC10 electrode at different temperatures and corresponding activation energy (E_a) are presented in Fig. 7. Obviously, R_p decreases with increasing temperatures, indicating that electrochemical processes occurring in the electrode are thermally activated. Increasing the amount of Yb dopant from 5 mol% to 10 mol% resulted in a decrease in R_p. The SYbC10 electrode demonstrates R_p of 0.051, 0.115 and 0.272 Ω cm^2 at 750, 700 and 650 ^{o}C, respectively, lower than that of the SYbC5 electrode. Activation energy of SYbC10 is 1.39 eV, which is also lower than that of SYbC5 electrode, that is 1.57 eV. This could be attributed to crystal structure evolution induced by the Yb dopant. As mentioned previously, with increasing doping content of Yb from 5 mol% to 10 mol%, a gradual structural transition took place from tetragonal structure with oxygen vacancy ordering towards disordered vacancies. Accordingly, SYbC10 possesses a structure similar to the ORR/OER active primitive cubic symmetry with disordered oxygen vacancies. This creates 3D pathways for oxygen ion transport, favoring electrode processes. The resulting lower R_p and E_a values obtained from the SYbC10 electrode, when compared to the SYbC5 electrode results, support this explanation.

3.3.2 Oxygen partial pressure dependent polarization resistance and electrochemical kinetics

ORR in porous SYbC10 electrode involves complicated multistep reactions. The reaction process is strongly dependent on oxygen pressures applied on electrode and determines electrode polarization resistance. Mathematically,

$$R_i = kP_{O_2}^{-m}, i = h,l \quad (4)$$

where, R is polarization resistance, k a constant, P_{O_2} oxygen partial pressure, m is reaction order and quantitatively related to each of multistep reactions as follows:

Step 1: molecular oxygen adsorption process onto porous electrode surface ($m = 1$)

$$O_{2,g} + SYbC10\ (s) \leftrightarrow O_{2,ads}(SYbC10) \quad (5)$$

Step 2: dissociation of adsorbed molecular oxygen into atomic oxygen ($m = 0.5$)

$$O_{2,ads}(SYbC10) \leftrightarrow 2O_{ads}(SYbC10) \quad (6)$$

Step 3: charge transfer reaction for oxygen anion formation and incorporation into oxygen vacancy ($m = 0.25$)

$$O_{ads}(SYbC10) + 2e^- + V_O^{\cdot\cdot} \leftrightarrow O_O^{\times} + SYbC10(s) \quad (7)$$

Fig. 8a shows the correlation between high frequency polarization and applied oxygen partial pressures at different temperatures. It can be seen that reaction orders *m* of 0.28, 0.23, 0.29, and 0.27 are obtained at 600, 650, 700, and 750 °C respectively, which are close to 0.25, suggesting that high frequency polarization is mainly associated with the charge transfer reaction process. Values of reaction order *m* for low frequency polarization are 0.48, 0.60, 0.57 and 0.59, respectively (Fig. 8b), indicating that the low frequency polarization is mainly associated with dissociation process of adsorbed oxygen into atomic oxygen. Accordingly, oxygen molecule dissociation and charge transfer processes are the two rate-limiting steps for the SYbC10 cathode material.

3.3.3 Electrochemical kinetic stability of SYbC10 cathode

Durability is critical for practical applications of SOFCs cathode materials. In this section, a durability test was carried out using a symmetrical cell with SYbC10 electrode at 700 °C in air for ~ 300 h. EIS was measured periodically during the test. The polarization resistance R_p was then derived from the fitted EIS data as described in the previous section. Fig. 9a shows time history of polarization resistances. It can be seen that R_p fluctuates in the first 50 hours, then increases a little bit between 50 and 175 h. Beyond 175 h, R_p gradually approaches an equilibrium state. Fig. 9b shows EIS curves measured at 0th, 52th, 113th, 263th, 309th hour respectively. The EIS arcs gradually increase with time and reach an equilibrium state by the end of the test. As mentioned above, polarization resistance of electrode is contributed by several steps in the ORR. This increase in electrode polarization resistance could be linked to specific ORR steps, through which the degradation mechanism of electrode might be identified. For this purpose, time history of high (R_h) and low (R_l) frequency polarization resistances were obtained from the EIS measurements and shown

in Fig. 10a and 10b respectively. The R_h data shows some scatter in the first 100 hours, but gradually stabilizes and reaches a value comparable to (actually a little bit lower than) the values recorded at the start of the durability test. Since high frequency polarization is associated with charge transfer process as confirmed above for oxygen anion formation and incorporation into oxygen vacancy, it is reasonable to assume that surface oxygen vacancy distribution and electronic structure near oxygen vacancies remain stable during the test. The fluctuations in the R_h data in the first 100 hours may be related to reorganization and stabilization of oxygen vacancy distribution on the electrode surface. The R_l data also fluctuates in the first 25 hours, but then slowly increases, and reaches a relatively stable value around 300th h. As mentioned above, low frequency polarization resistance is closely related to the dissociation process of adsorbed oxygen molecule into atomic oxygen. Certainly, the dissociation process is effected by the surface catalytic property of the electrode, so it is reasonable to assume that the increase of R_l could be induced by a change in electrode surface characteristics. For ABO_3 perovskites, both A-site and B-site elements could be exsolved onto the bulk surface in long-term thermal treatment condition.[23, 37-41] As shown in Fig. 5, no any secondary phase can be found in XRD results of SYbC10 powders after 250 h thermal treatment, implying that either no element was exsolved from A-/B-sites or the amount of surface element exsolution was below the level detectable by the XRD. On the other hand, surface nano-particles are observed from the SEM image of SYbC10 electrode after the durability test (Fig. S5b), indicating that some elements were indeed exsolved. It has been widely demonstrated that transition metal exsolution from the B-site usually improves catalytic property or surface exchange rate of the material.[42, 43] However, the increase of R_l shown in Fig. 10b indicates that this is less likely the case. Therefore, the surface nano-particles in Fig. S5b is most likely induced by the element exsolution from the A-site. In $Sr_{1-x}Yb_xCoO_{3-\delta}$, the size mismatch between dopant and host cations induces elastic energy in crystals. During long-term thermal treatment process, such an elastic energy may drive cation rearrangement, resulting in surface Sr segregation. Ideal cubic $SrCoO_{3-\delta}$ consists of SrO and CoO_2 planes alternating stacking with -(SrO-CoO_2)$_n$- sequences. The Sr and Co cations have charges of 2+ and 4+, respectively, leading to neutral charge of $Sr^{2+}O^{2-}$ [0] and $Co^{4+}O_2^{2-}$ [0] planes.

However, Yb with charge of +3 makes positive charge of $Yb^{3+}O^{2-}$ [+1] in the AO planes and potential formation of negatively charged $Co^{3+}O_2^{2-}$ [-1] in the BO_2 planes. The alternating stacking of the charged AO and BO_2 planes would result in polar surface, which in turn could electrostatically drive surface cation segregation. Due to the lower surface energy of SrO surface[44, 45], SrO-terminated surface is prone to be formed with segregated Sr. Therefore, surface Sr segregation of $Sr_{1-x}Yb_xCoO_{3-\delta}$ could be induced by both elastic force and electrostatic force during long-term thermal treatment. To keep charge neutrality, surface oxygen vacancies will be created. This process can be expressed as,

$$Sr_{Sr}^{\times} + O_O^{\times} \leftrightarrow V_{Sr}'' + V_O^{\cdot\cdot} + SrO_{surface} \quad (8)$$

The created surface oxygen vacancies via surface Sr segregation will improve surface oxygen exchange rate and ORR kinetics. However, when the amount of Sr segregation is beyond a certain level, it might block the neighboring oxygen vacancies and reaction sites.[46, 47] These understanding may explain the time history of R_l. In the first 10 hours, R_l shows a rapid decrease likely due to a small amount of surface Sr segregation. Beyond ~10^{th} h, the amount of surface Sr segregation increases, leading to gradual increase of R_l values. The R_l data stabilizes around the 300^{th} h, implying that surface Sr segregation reaches an equilibrium state. It seems that the increase of overall polarization resistance R_p during the durability test is primarily induced by the increase of R_l, and therefore performance degradation could be mainly caused by surface Sr segregation.

3.3.4 CO_2 tolerance and recovery capability of SYbC10 cathode

Gas supplied to cathode electrodes of SOFCs may contain a small amount of CO_2 especially air from the surrounding ambient atmosphere. Even though CO_2 content is very low, it may easily adsorb onto cathode surface, forming several types of surface adsorbates. Surface adsorbed CO_2 could even react with cathode material, resulting in surface secondary phases.[48] This usually occurs for Sr containing perovskite cathodes, where surface oxo-carbonaceous species are formed at elevated temperatures, such as adventitious-like carbon species, monodentate carbonate, bidentate carbonate and carbonate species.[49, 50]

Such surface oxo-carbonaceous species block ORR active sites and deteriorate surface (electro)catalytic properties, causing degradation of cathode electrodes. Although degradation alleviation is possible by annealing at a relatively high temperature, e.g., decomposition of $SrCO_3$ in air[51, 52] and desorption of surface oxo-carbonaceous species, the high temperature process may induce other problems such as microstructure coarsening of electrodes and unwanted side reactions at interfaces within the device, which make it difficult to recover to its initial state and performance. In this section, stability and recovery capability of SYbC10 as cathode material is evaluated using a symmetrical cell in CO_2-containing atmosphere at elevated temperatures. For this test, a symmetrical cell SYbC10/SDC/SYbC10 was sealed in an alumina tube chamber. Pure air and 5% CO_2-containing air were supplied into the chamber alternatively every 2 hours for the first 12 hours. After 12 hours, pure air was constantly supplied into the chamber without switching to CO_2 containing air. EIS was measured every half hour during the testing. R_o and R_p were then extracted from the EIS data. Fig. 11 shows the time history of R_o and R_p at 700 and 650 ^oC respectively. It can be seen that at 700 ^oC, the ohmic resistance remained stable for the first ~ 7 hours, then showed a small increase, and stayed unchanged for the remainder of the test (Fig. 11a). It did not show any obvious variations following the applied cycling between pure air and 5% CO_2-air. This observation indicates that variations in R_O are mainly induced by the thermal ageing process, in which the cell may experience microstructure evolution during the course of stability test at 700 ^oC. The polarization resistance in Fig. 11b clearly shows fluctuations that followed the applied cycles of surrounding gas atmosphere. R_p was relatively low in pure air but quickly increased to a high value once gas atmosphere was switched to 5% CO_2-air. This result indicates that SYbC10 material is very sensitive to CO_2 but reversible from CO_2-contaminated state. Interestingly, after a few gas cycles, R_p becomes lower than the initial value, implying that surface phase/microstructure favoring electro-catalytic property of electrode could be formed, which is not completely clear at this stage. In addition to potential adsorption/desorption of surface carbonaceous species, it is assumed that following surface reactions are occurring:

$$Sr_{0.9}Yb_{0.1}CoO_{3-\delta} + xCO_2 \rightarrow xSrCO_3 + Sr_{0.9-x}Yb_{0.1}CoO_{3-\delta}\ (in\ 5\%\ CO_2\ containing\ air) \quad (9)$$

$$SrCO_3 + O_2 \rightarrow SrO + CO_2 \ \ (in\ pure\ air) \quad (10)$$

At the temperature of 700 °C, Sr segregation first occurs and appears on the cathode surface. When CO_2 is adsorbed onto the cathode surface, the surface segregated Sr and/or lattice Sr is converted into $SrCO_3$ (reaction 9). Fig. S6 shows XRD patterns of SYbC10 powders after treated in 5% CO_2-air for 2 h at 650 and 700 °C respectively followed by cooling down under the protection of nitrogen gas. It can be seen that the peaks corresponding to $SrCO_3$ phase occurred. This result confirms the assumption that CO_2 did react with Sr in SYbC10, forming $SrCO_3$ phase. After switching to pure air, the chemisorbed surface carbonaceous species are desorbed and the formed $SrCO_3$ is decomposed into SrO and CO_2 at 700 °C (reaction 10). In fact, after SYbC10 powders were treated at 700 in 5% CO_2-air for 2 h followed by treatment in pure air for another 2 h at 700 °C, $SrCO_3$ phase completely disappeared but SrO phase appeared as shown in Fig. S7. After a few gas cycles, the nano-porous surface and/or surface micro-composition that favors ORRs on the electrode may be formed, leading to the smaller values of R_p. At a lower temperature of 650 °C, the variations in ohmic resistance synchronize with the cycles of applied gas atmosphere (Fig. 11c). Interestingly, R_o was slightly larger during the pure air portion of the cycle than in the 5% CO_2-air portion of the cycle. Variation in polarization resistance also followed the cycles of applied gas atmosphere, low in pure air cycle but high in 5% CO_2-air cycle (Fig. 11d). While R_p remained relatively constant in pure air after the first gas cycle; in 5% CO_2-air, it increased by ~350% of its initial value, but began decreasing following every subsequent gas cycle. After air treatment, R_p at the 28th h showed a little higher value than its initial one before the cycling test.

Based on above analysis and experimental results, one can see that R_p variations of SYbC10 electrode are attributed to two major surface factors during the atmosphere switching between pure air and 5% CO_2-air: one is surface oxo-carbonaceous species, e.g., adventitious-like carbon and (bi)carbonate species, induced by direct chemisorption of CO_2; another is surface $SrCO_3$ phase formed by chemical reaction of Sr and CO_2. At elevated temperatures, SYbC10 electrode will lose oxygen and generate more oxygen vacancies. It has been reported that surface oxygen vacancy is the acidic center for the adsorption of CO_2.[53]

This may lead to more CO_2 reacting with surface Sr, forming $SrCO_3$ phase in 5% CO_2-air since perovskite with more oxygen vacancies is more susceptible to CO_2.[54] It is reasonable to assume that the amount of $SrCO_3$ phase formed at 700 °C will be more than that at 650 °C. This understanding is confirmed by XRD results in Fig. S6, where after SYbC10 powders were treated in 5% CO_2-air for 2 h at 650 and 700 °C respectively, the secondary phase of $SrCO_3$ was formed. And the relative peak intensity of $SrCO_3$ at 700 °C is stronger than that at 650 °C, indicating that the formation of strontium carbonates is more favorited at higher temperatures for SYbC10. On the other hand, it has been recognized that surface oxo-carbonaceous species, e.g., adventitious-like carbon and (bi)carbonate species, are favorably chemisorbed at lower temperatures.[49] In other words, it is difficult to desorb such surface oxo-carbonaceous species at lower temperatures. Both the formed surface strontium carbonate and chemisorbed surface oxo-carbonaceous species will block reaction sites for surface oxygen exchange. Since the formed surface strontium carbonate and chemisorbed surface oxo-carbonaceous species are sensitive to operating temperatures, the combinational effect of these two surface factors leads to different R_p behaviors at 650 °C from those at 700 °C. This could be the reason that the increase of R_p (or the increase ratio of R_p relative to its initial value) at 650 °C is bigger than that at 700 °C when the atmosphere is switched from pure air to 5% CO_2-air (Fig. 11). After the atmosphere is switched from 5% CO_2-air back to pure air, R_p at 700 °C rapidly recovers and reaches a value that is a little bit lower than its initial one (Fig.11b). This result implies that not only the chemisorbed surface carbonaceous species are completely desorbed but also the formed surface strontium carbonates are fully decomposed. Meanwhile, the decomposition of surface strontium carbonates might also introduce porous nano-surface structures favoring ORRs. By contrast, R_p at 650 °C shows only partial recovery and reaches a value that is higher than its initial one (Fig.11d). This observation indicates that the chemisorbed surface oxo-carbonaceous species are not completely desorbed and/or the formed surface strontium carbonates are not completely decomposed at 650 °C after the atmosphere is changed back to pure air from 5% CO_2-air. As a consequence, the surface ORR sites of SYbC10 electrodes are still partially blocked. The non-complete recovery of ORR sites also leads to a hysteresis behavior in the cell

resistance at 650 °C during the atmosphere cycles between pure air and 5% CO_2-air. In open literatures, the R_p of the widely-studied $Ba_{0.5}Sr_{0.5}Co_{0.8}Fe_{0.2}O_{3-\delta}$ (BSCF)[26] may reach 9 times its initial value after being exposed to 10% CO_2 for 15 min at 700 °C, and 27 times its initial value after being exposed to 5% CO_2 for 15 min at 600 °C. The maximum R_p of SYbC10 developed in this paper only reached ~ 2.1 times (Fig. 11b) and 4.5 times (Fig. 11d) at 700 °C and 650 °C respectively after being exposed to 5% CO_2 for 30 min. This simple comparison indicates that SYbC10 has good property for CO_2 tolerance. The partial substitution of Sr by Yb with higher electronegativity on A-site is able to mitigate CO_2 adsorption onto SYbC10 electrode surface.

V. Conclusion

A new series of $Sr_{1-x}Yb_xCoO_{3-\delta}$ (x = 0, 0.05, 0.10 and 0.15) with different Yb doping concentrations has been synthesized and systematically characterized. Results indicate that $Sr_{0.95}Yb_{0.05}CoO_{3-\delta}$ and $Sr_{0.90}Yb_{0.10}CoO_{3-\delta}$ samples possess a tetragonal superstructure phase with oxygen vacancy ordering (*I4/mmm*; $2a_c \times 2a_c \times 4a_c$). With increasing the amount of Yb doping level, the phases demonstrate a transition tendency towards cubic structure with disordered oxygen vacancies. Both SYbC5 and SYbC10 phases show excellent thermal stability at 700 °C. Due to the less ordered oxygen vacancies, SYbC10 demonstrates very good ORR activity with polarization resistance of 0.051, 0.115 and 0.272 Ω cm^2 at 750, 700 and 650 °C, respectively. Dissociation of adsorbed oxygen and charge transfer processes are the two rate-limiting steps in the ORR for the SYbC10 cathode. Durability testing (~ 300 h) in combination with EIS analysis indicates that surface oxygen vacancy distribution and electronic structure near oxygen vacancies are very stable but dissociation of adsorbed oxygen molecule into atom oxygen process is affected by surface Sr segregation, and polarization resistance degradation is mainly induced by surface Sr segregation. SYbC10 is very sensitive to CO_2 containing atmospheres. At a relatively high temperature of 700 °C, the polarization resistance closely follows the cycles between pure air and CO_2-air and has a relatively higher values during CO_2-air portion of the cycle. This effect is temporary and polarization

performance completely recovers in pure air cycle, likely due to complete desorption of surface oxo-carbonaceous species and decomposition of surface carbonates. The polarization resistance after a few gas cycle treatments becomes lower than that before the CO_2 treatment, probably due to surface nanostructures induced by cyclic formation and decomposition of surface carbonates. At a relatively low temperature of 650 ^oC, the polarization resistance still follows the same cyclic behavior, but complete recovery from CO_2-air portion of cycle is not observed, leading to hysteresis behavior likely due to non-complete desorption of surface oxo-carbonaceous species and/or non-complete decomposition of surface carbonates after switching to pure air portion of cycle. After a few pure air to 5% CO_2-air cycles at 650 ^oC, the polarization resistance of SYbC10 electrode increases from the initial data in pure air. This work provides a promising strategy to stabilize $SrCoO_{3-\delta}$ through a simple cation doping method while obtaining very good electrochemical kinetic properties and stability of the material. The material developed in this study can be used as an alternative cathode for intermediate temperature SOFCs toward commercial applications.

Acknowledgement

This work was supported by the U.S. Department of Energy through National Energy Technology Laboratory under grant number DE-FE0031473 and DE-FE0024059.

References

1. D. J. Brett, A. Atkinson, N. P. Brandon and S. J. Skinner, *Chem. Soc. Rev.*, 2008, **37**, 1568-1578.
2. E. D. Wachsman and K. T. Lee, *Science*, 2011, **334**, 935-939.
3. N. Q. Minh, *J. Am. Ceram. Soc.*, 1993, **76**, 563-588.
4. T. Komatsu, R. Chiba, H. Arai and K. Sato, *J. Power Sources*, 2008, **176**, 132-137.
5. J. Richter, P. Holtappels, T. Graule, T. Nakamura and L. J. Gauckler, *Monatshefte für Chemie-Chemical Monthly*, 2009, **140**, 985-999.
6. A. F. Sammells, R. L. Cook, J. H. White, J. J. Osborne and R. C. MacDuff, *Solid State Ionics*, 1992, **52**, 111-123.
7. D. Chen, C. Chen, Z. Zhang, Z. M. Baiyee, F. Ciucci and Z. Shao, *ACS Appl. Mater. Interfaces*, 2015, **7**, 8562-8571.
8. C. De la Calle, A. Aguadero, J. Alonso and M. Fernández-Díaz, *Solid State Sci.*, 2008, **10**, 1924-1935.
9. H. Kruidhof, H. J. Bouwmeester, R. v. Doorn and A. Burggraaf, *Solid State Ionics*, 1993, **63**, 816-822.
10. W. Zhou, Z. Shao, R. Ran and R. Cai, *Electrochem. Commun.*, 2008, **10**, 1647-1651.
11. R. D. Shannon, *Acta Crystallogr. A*, 1976, **32**, 751-767.
12. D. Chen, C. Chen, Y. Gao, Z. Zhang, Z. Shao and F. Ciucci, *J. Power Sources*, 2015, **295**, 117-124.
13. F. Wang, Q. Zhou, T. He, G. Li and H. Ding, *J. Power Sources*, 2010, **195**, 3772-3778.
14. W. Zhou, J. Sunarso, M. Zhao, F. Liang, T. Klande and A. Feldhoff, *Angew. Chem. Int. Ed.*, 2013, **52**, 14036-14040.
15. Y. Shen, F. Wang, X. Ma and T. He, *J. Power Sources*, 2011, **196**, 7420-7425.
16. A. Aguadero, J. A. Alonso, D. Pérez-Coll, C. de la Calle, M. a. T. Fernández-Díaz and J. B. Goodenough, *Chem. Mater.*, 2009, **22**, 789-798.

17. A. Aguadero, D. Pérez-Coll, J. Alonso, S. Skinner and J. Kilner, *Chem. Mater.*, 2012, **24**, 2655-2663.

18. M. Li, W. Zhou, V. K. Peterson, M. Zhao and Z. Zhu, *J. Mater. Chem. A*, 2015, **3**, 24064-24070.

19. G. López-Pacheco, R. López-Juárez, M. E. Villafuerte-Castrejón, C. Falcony, E. Barrera-Calva and F. González, *Dalton Trans.*, 2019, **48**, 11889-11896.

20. Y. Wang, L. Li, J. Qi and Z. Gui, *Ceram. Int.*, 2002, **28**, 657-661.

21. S. W. Park, B. K. Moon, S. H. Park, J. H. Jeong, H. Choi and J. H. Kim, *RSC Advances*, 2017, **7**, 1464-1470.

22. G. M. Rupp, A. K. Opitz, A. Nenning, A. Limbeck and J. Fleig, *Nat. Mater.*, 2017, **16**, 640.

23. Y. Li, W. Zhang, Y. Zheng, J. Chen, B. Yu, Y. Chen and M. Liu, *Chem. Soc. Rev.*, 2017, **46**, 6345-6378.

24. H. Yokokawa, H. Tu, B. Iwanschitz and A. Mai, *J. Power Sources*, 2008, **182**, 400-412.

25. M. Arnold, H. Wang and A. Feldhoff, *J. Membr. Sci.*, 2007, **293**, 44-52.

26. Y. Zhang, G. Yang, G. Chen, R. Ran, W. Zhou and Z. Shao, *ACS Appl. Mater. Interfaces*, 2016, **8**, 3003-3011.

27. H. Zhao, N. Xu, Y. Cheng, W. Wei, N. Chen, W. Ding, X. Lu and F. Li, *J. Phys. Chem. C*, 2010, **114**, 17975-17981.

28. W. Gordy and W. O. Thomas, *J. Chem. Phys.*, 1956, **24**, 439-444.

29. B. H. Toby and R. B. Von Dreele, *J. Appl. Crystallogr.*, 2013, **46**, 544-549.

30. R. Le Toquin, W. Paulus, A. Cousson, C. Prestipino and C. Lamberti, *J. Am. Chem. Soc.*, 2006, **128**, 13161-13174.

31. Y. Ito, R. F. Klie, N. D. Browning and T. J. Mazanec, *J. Am. Ceram. Soc.*, 2002, **85**, 969-976.

32. R. E. Usiskin, T. C. Davenport, R. Y. Wang, W. Guan and S. M. Haile, *Chem. Mater.*, 2016, **28**, 2599-2608.

33. W. T. Harrison, S. L. Hegwood and A. J. Jacobson, *J. Chem. Soc., Chem. Commun.*, 1995, 1953-1954.

34. T. Nagai, W. Ito and T. Sakon, *Solid State Ionics*, 2007, **177**, 3433-3444.

35. M. James, D. Cassidy, D. Goossens and R. Withers, *J. Solid State Chem.*, 2004, **177**, 1886-1895.

36. Y. Li, Y. N. Kim, J. Cheng, J. A. Alonso, Z. Hu, Y.-Y. Chin, T. Takami, M. T. Fernández-Díaz, H.-J. Lin and C.-T. Chen, *Chem. Mater.*, 2011, **23**, 5037-5044.

37. L. Zhao, J. Drennan, C. Kong and S. Amarasinghe, *J. Mater. Chem. A*, 2014, **2**, 11114-11123.

38. F. S. Baumann, J. Fleig, M. Konuma, U. Starke, H.-U. Habermeier and J. Maier, *J. Electrochem. Soc.*, 2005, **152**, A2074-A2079.

39. M. Liu, D. Ding, K. Blinn, X. Li, L. Nie and M. Liu, *Int. J. Hydrogen Energy*, 2012, **37**, 8613-8620.

40. B. Koo, K. Kim, J. K. Kim, H. Kwon, J. W. Han and W. Jung, *Joule*, 2018, **2**, 1476-1499.

41. S. Chen, Y.-Q. Su, P. Deng, R. Qi, J. Zhu, J. Chen, Z. Wang, L. Zhou, X. P. Guo and B. Y. Xia, *ACS Catal.*, 2020, **10**, 4640-4646.

42. H. Zhang and W. Yang, *Chem. Commun. (Cambridge, U. K.)*, 2007, 4215-4217.

43. D. Chen, C. Huang, R. Ran, H. J. Park, C. Kwak and Z. Shao, *Electrochem. Commun.*, 2011, **13**, 197-199.

44. H. Ding, A. V. Virkar, M. Liu and F. Liu, *Phys. Chem. Chem. Phys.*, 2013, **15**, 489-496.

45. J. Druce, H. Tellez, M. Burriel, M. Sharp, L. Fawcett, S. Cook, D. McPhail, T. Ishihara, H. Brongersma and J. Kilner, *Energy Environ. Sci.*, 2014, **7**, 3593-3599.

46. E. J. Crumlin, E. Mutoro, Z. Liu, M. E. Grass, M. D. Biegalski, Y.-L. Lee, D. Morgan, H. M. Christen, H. Bluhm and Y. Shao-Horn, *Energy Environ. Sci.*, 2012, **5**, 6081-6088.

47. E. Mutoro, E. J. Crumlin, M. D. Biegalski, H. M. Christen and Y. Shao-Horn, *Energy Environ. Sci.*, 2011, **4**, 3689-3696.

48. Y.-L. Huang, C. Pellegrinelli, M. Sakbodin and E. D. Wachsman, *ACS Catal.*, 2018, **8**, 1231-1237.

49. J. Hwang, R. R. Rao, Y. Katayama, D. Lee, X. R. Wang, E. Crumlin, T. Venkatesan, H. N. Lee and Y. Shao-Horn, *J. Phys. Chem. C*, 2018, **122**, 20391-20401.

50. J. M. Tascón and L. G. Tejuca, *J. Chem. Soc. Faraday Trans. 1 Phys. Chem. Condens. Phases*, 1981, **77**, 591-602.

51. K. Efimov, T. Klande, N. Juditzki and A. Feldhoff, *J. Membr. Sci.*, 2012, **389**, 205-215.

52. A. Yan, M. Cheng, Y. Dong, W. Yang, V. Maragou, S. Song and P. Tsiakaras, *Appl. Catal. B*, 2006, **66**, 64-71.

53. Y. Zhu, J. Sunarso, W. Zhou and Z. Shao, *Appl. Catal. B*, 2015, **172**, 52-57.

54. K. Nomura, Y. Ujihira, T. Hayakawa and K. Takehira, *Appl. Catal. A*, 1996, **137**, 25-36.

Figure Captions

Fig.1 XRD patterns of $Sr_{1-x}Yb_xCoO_{3-\delta}$ (x = 0, 0.05, 0.10 and 0.15) powders calcinated at 1000 ^oC in air for 6 h, peak positions of $Sr_6Co_5O_{15}$, and Co_3O_4 and indices of simple cubic structure $SrCoO_{3-\delta}$ (*Pm-3m*, JCPDS 38-1148).

Fig. 2 Magnified XRD patterns of SYbC5 and SYbC10 powders calcinated at 1000 ^oC in air for 6 h: (a) 2θ = 38-56^o; (b) $(200)_c$, $(211)_c$, $(220)_c$ peaks.

Fig. 3 Rietveld refinement plot of SYbC5 (a) and SYbC10 (b) powders at room temperature using XRD data.

Fig. 4 High-resolution TEM images of SYbC5 (a) and SYbC10 (b) powders after high energy ball milling and interplanar distance of SYbC5 (c) and SYbC10 (d) powders.

Fig. 5 XRD patterns of SYbC5 and SYbC10 powders before and after annealing treatment at 700 ^oC in air for 250 h.

Fig. 6 Typical Nyquist (a) and Bode (b) plots of symmetrical cells with SYbC5 and SYbC10 electrode measured at 700 ^oC in air. The inset is an equivalent circuit model used for curve fitting.

Fig. 7 Polarization resistance *vs* 1000/T of SYbC5 and SYbC10 electrode measured in air from 750-600 ^oC.

Fig. 8 Correlations between R_h (a), R_l (b) and applied oxygen partial pressures at different temperatures.

Fig. 9 Long-term stability of SYbC10/SDC/SYbC10 symmetrical cell in air at 700 ^oC: (a) time history of polarization resistance, (b) evolution of EIS at selected measurement points.

Fig. 10 Time history of polarization resistance associated with high frequency (a) and low frequency (b) process for SYbC10 cathode at 700 ^oC in air.

Fig. 11 Time history of ohmic and polarization resistance evolution curves of SYbC10 electrode in applied gas cycles between air and 5% CO_2-air at 700 (a and b) and 650 ^oC (c and d).

Table 1 Structure parameters and R-factors for SYbC5 and SYbC10 derived from Rietveld refinement using XRD data at room temperature.

	x = **0.05**	x = **0.10**
a_t (Å)	7.6944(7)	7.6813(0)
c_t (Å)	15.4117(7)	15.3809(7)
$c_t/2a_t$	1.00147(9)	1.00119(5)
V(Å^3)	912.453	907.513
χ^2	6.29	4.67
R_{wp} (%)	3.01	2.26
$R_F{}^2$ (%)	6.02	2.63

Fig.1

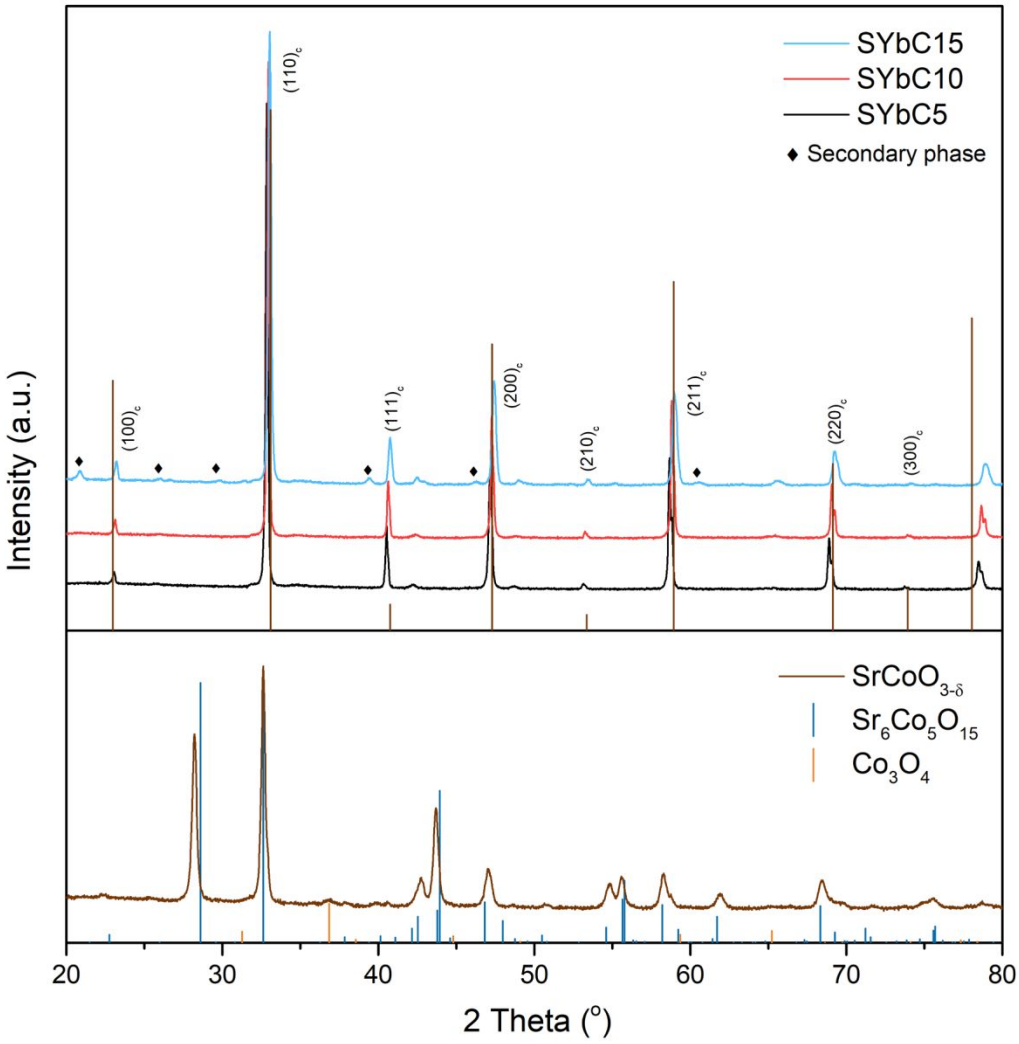
SYbC15
SYbC10
SYbC5
♦ Secondary phase
(100)c
(110)c
(111)c
(200)c
(210)c
(211)c
(220)c
(300)c
Intensity (a.u.)
SrCoO3-δ
Sr6Co5O15
Co3O4
20
30
40
50
60
70
80
2 Theta (°)

Fig. 2

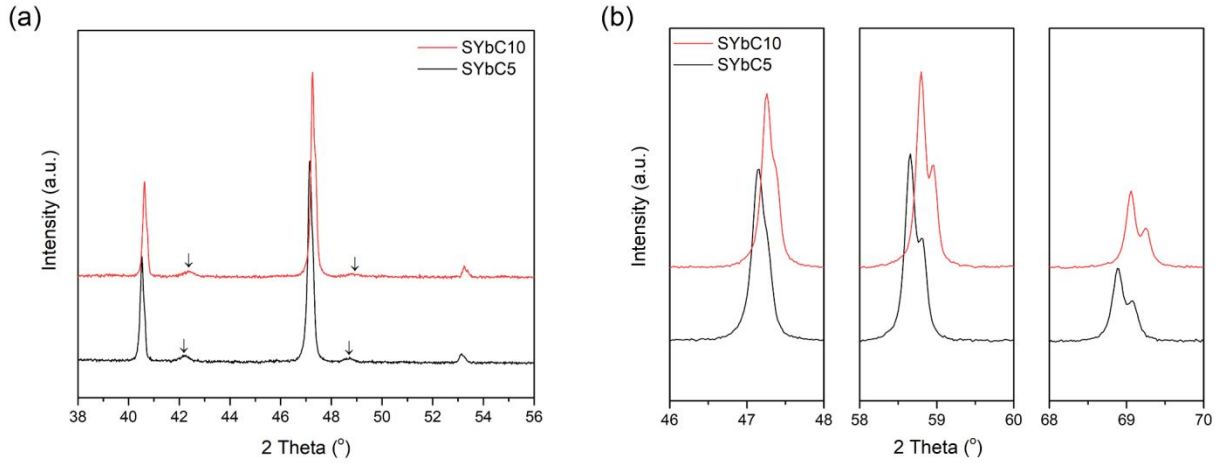
(a)
SYbC10
SYbC5
Intensity (a.u.)
38
40
42
44
46
48
50
52
54
56
2 Theta (°)
(b)
SYbC10
SYbC5
Intensity (a.u.)
46
47
48
58
59
60
68
69
70
2 Theta (°)

Fig. 3

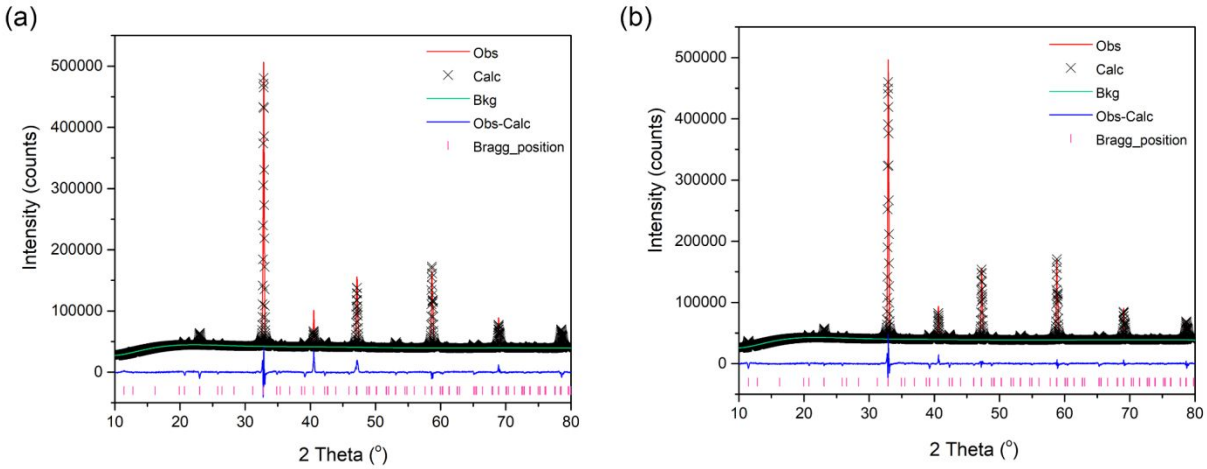
(a)
Obs
Calc
Bkg
Obs-Calc
Bragg_position
Intensity (counts)
2 Theta (°)
(b)
Obs
Calc
Bkg
Obs-Calc
Bragg_position
Intensity (counts)
2 Theta (°)

Fig. 4

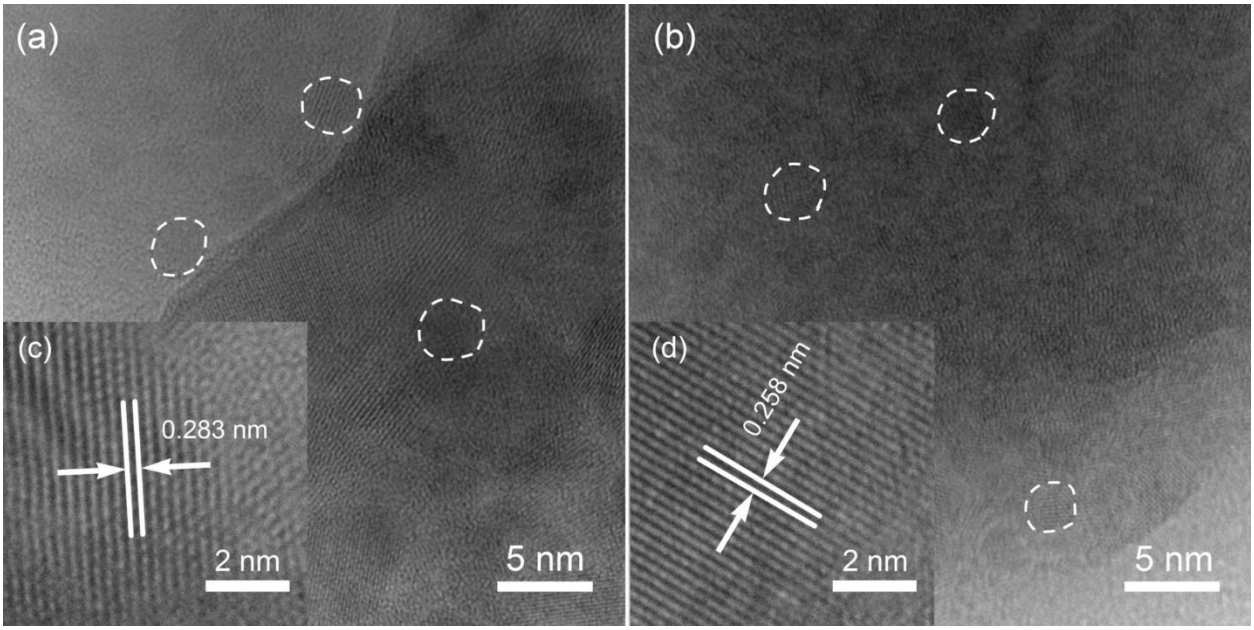

Fig. 5

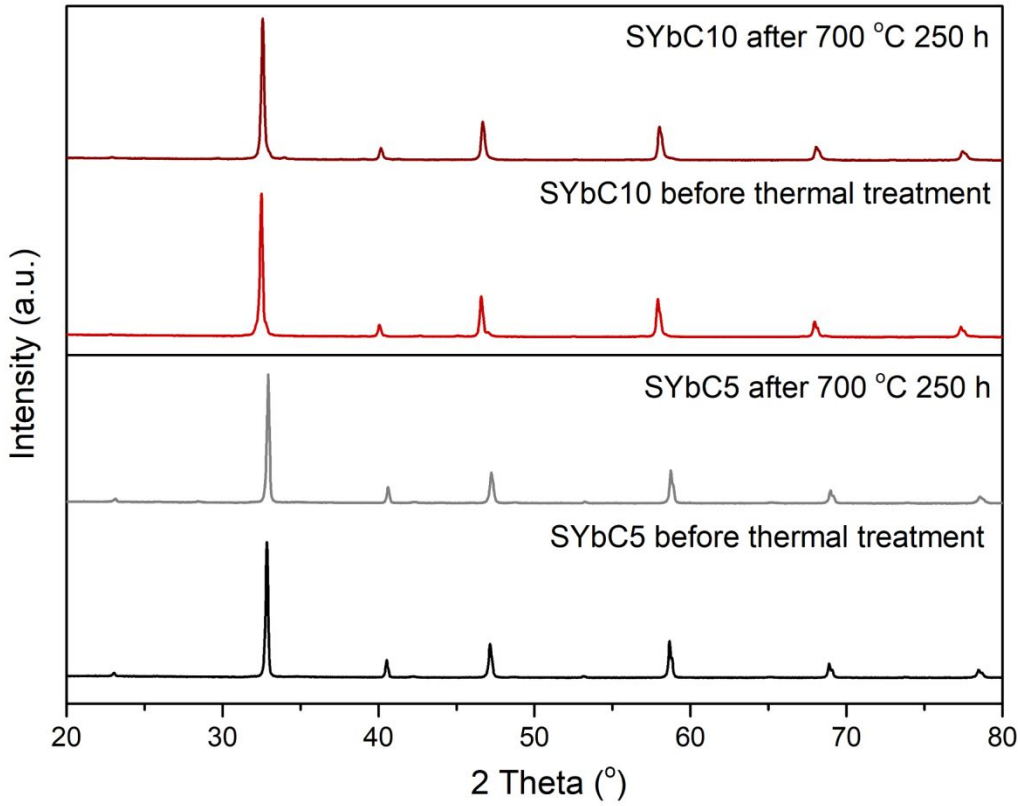
SYbC10 after 700 °C 250 h
SYbC10 before thermal treatment
SYbC5 after 700 °C 250 h
SYbC5 before thermal treatment
Intensity (a.u.)
20
30
40
50
60
70
80
2 Theta (°)

Fig. 6

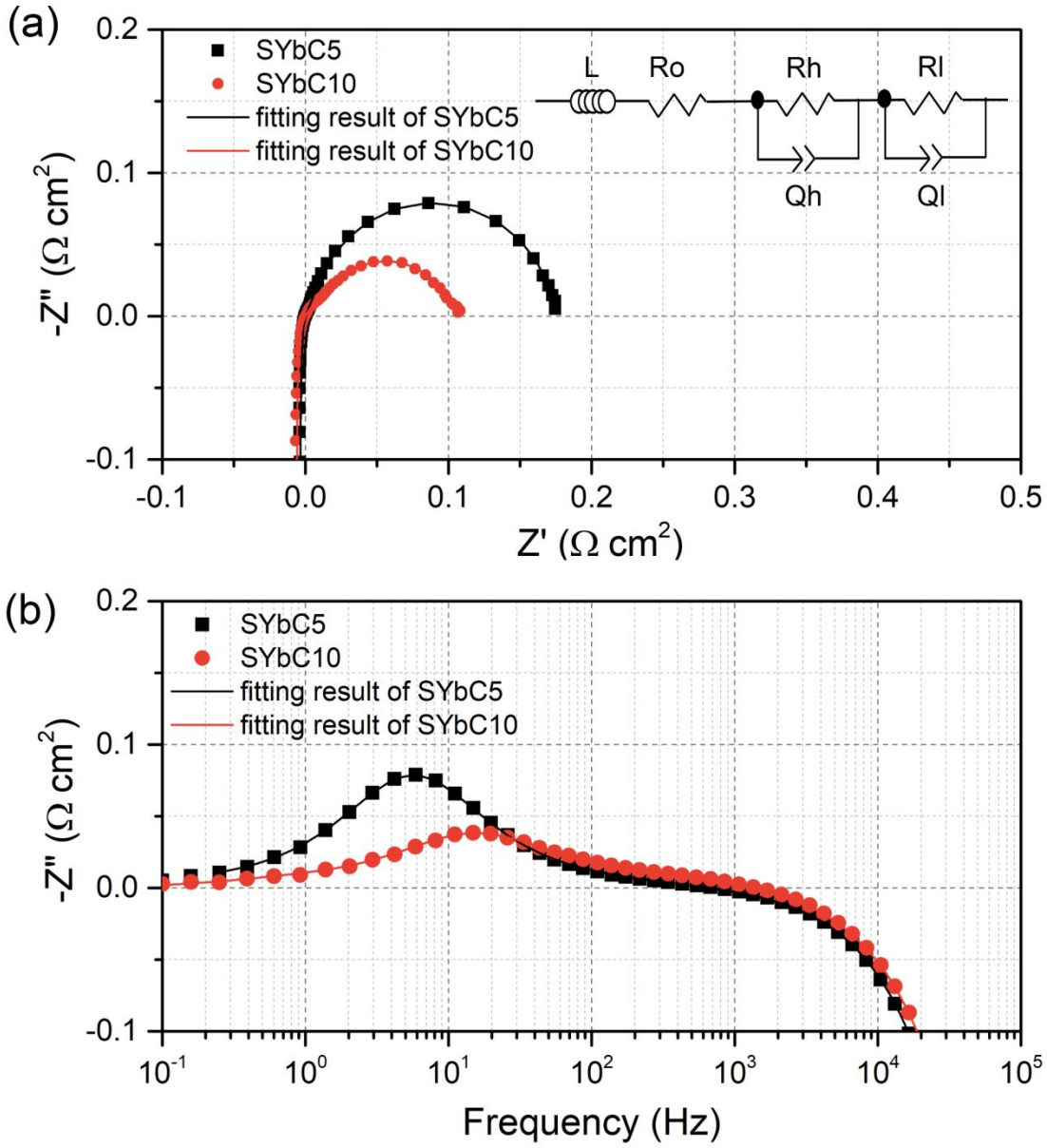
(a)
SYbC5
SYbC10
fitting result of SYbC5
fitting result of SYbC10
L
Ro
Rh
Rl
Qh
Ql
-Z'' (Ω cm2)
Z' (Ω cm2)
(b)
SYbC5
SYbC10
fitting result of SYbC5
fitting result of SYbC10
-Z'' (Ω cm2)
Frequency (Hz)

Fig. 7

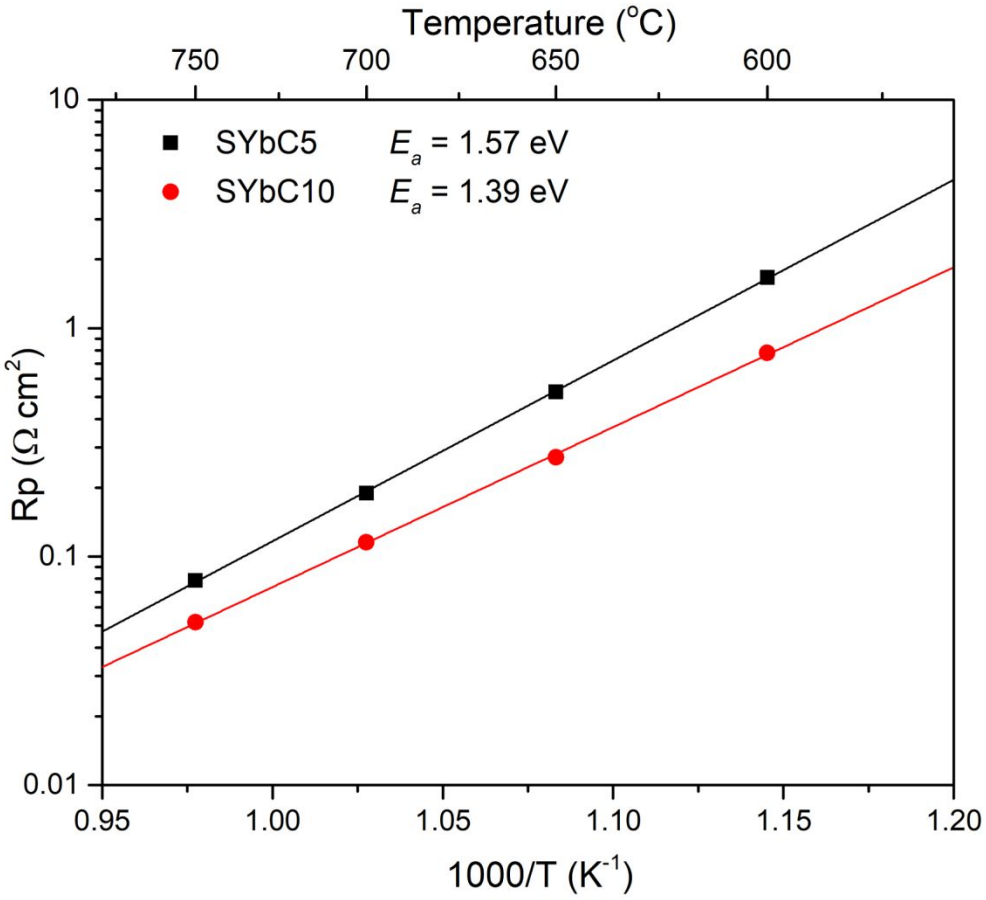
Temperature (°C)
750
700
650
600
10
1
0.1
0.01
Rp (Ω cm²)
SYbC5
E_a = 1.57 eV
SYbC10
E_a = 1.39 eV
0.95
1.00
1.05
1.10
1.15
1.20
1000/T (K⁻¹)

Fig. 8

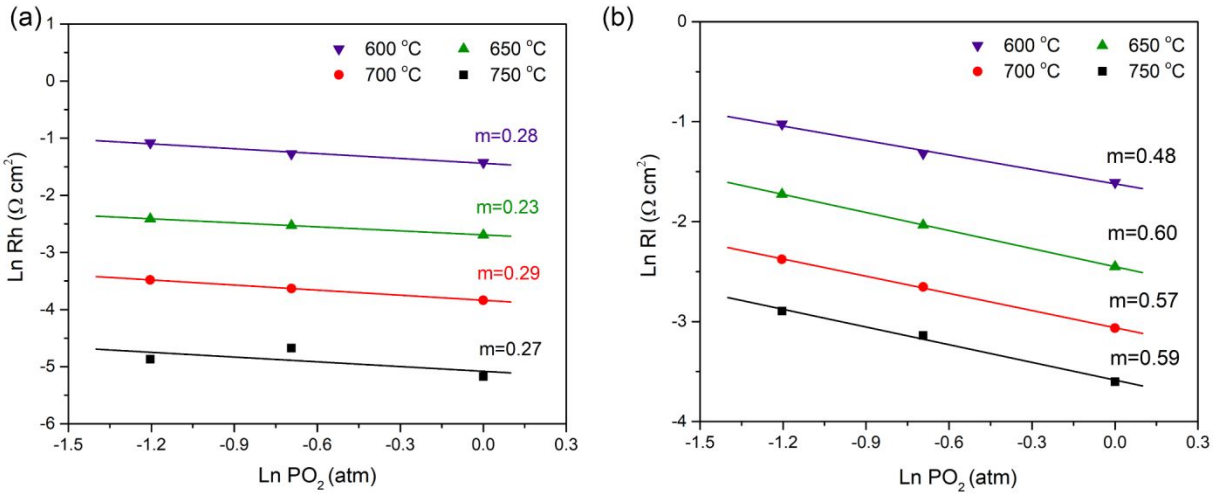
(a)
600 °C
650 °C
700 °C
750 °C
m=0.28
m=0.23
m=0.29
m=0.27
Ln Rh (Ω cm²)
Ln PO₂ (atm)
(b)
600 °C
650 °C
700 °C
750 °C
m=0.48
m=0.60
m=0.57
m=0.59
Ln Rl (Ω cm²)
Ln PO₂ (atm)

Fig. 9

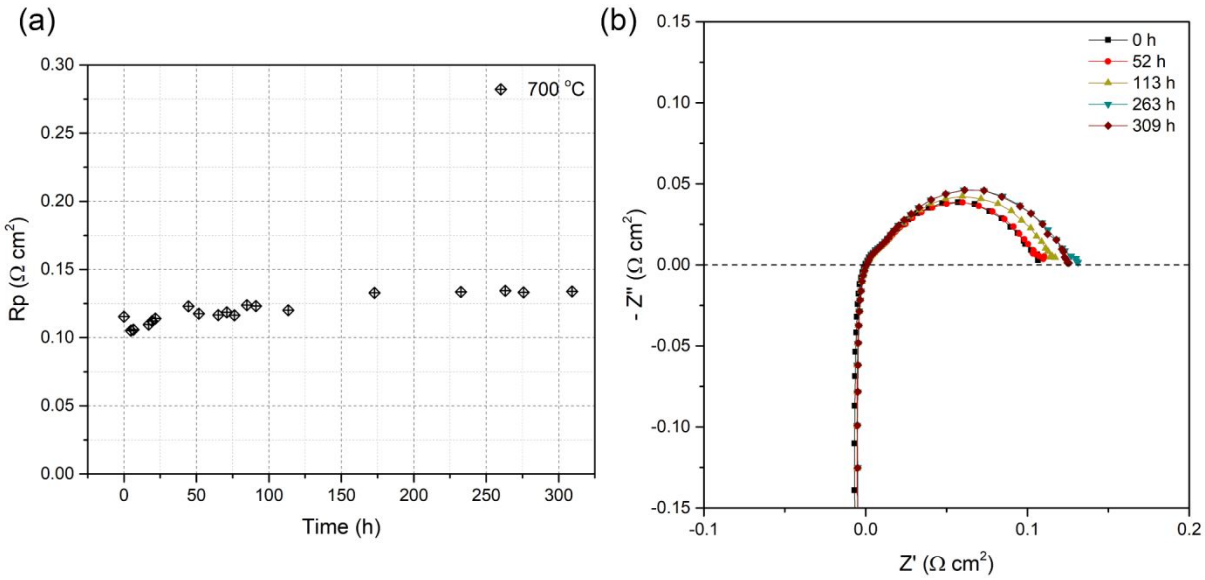
(a)
700 °C
Rp (Ω cm²)
Time (h)
0.30
0.25
0.20
0.15
0.10
0.05
0.00
0
50
100
150
200
250
300
(b)
0 h
52 h
113 h
263 h
309 h
- Z'' (Ω cm²)
Z' (Ω cm²)
0.15
0.10
0.05
0.00
-0.05
-0.10
-0.15
-0.1
0.0
0.1
0.2

Fig. 10

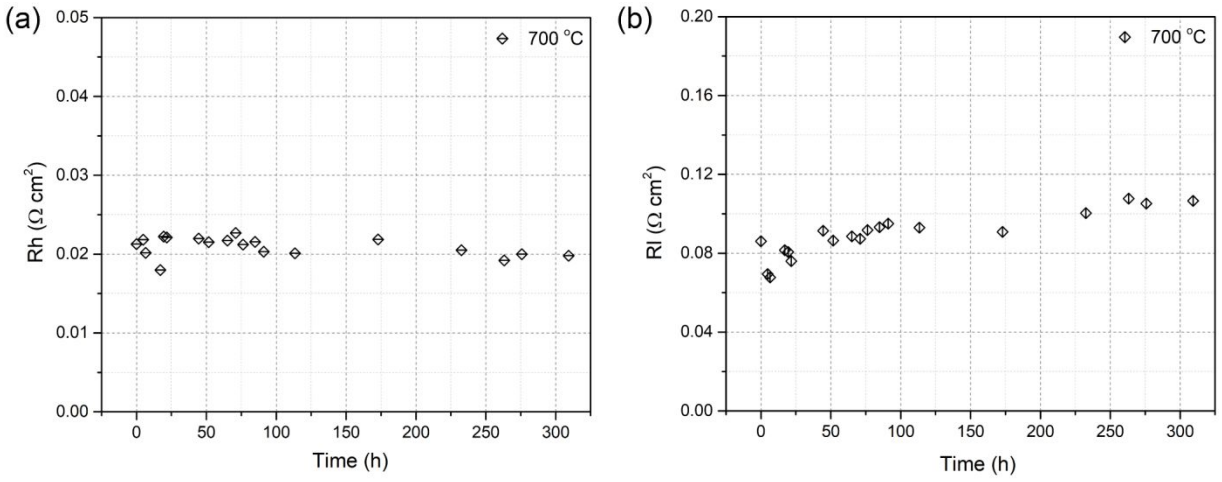

Fig. 11

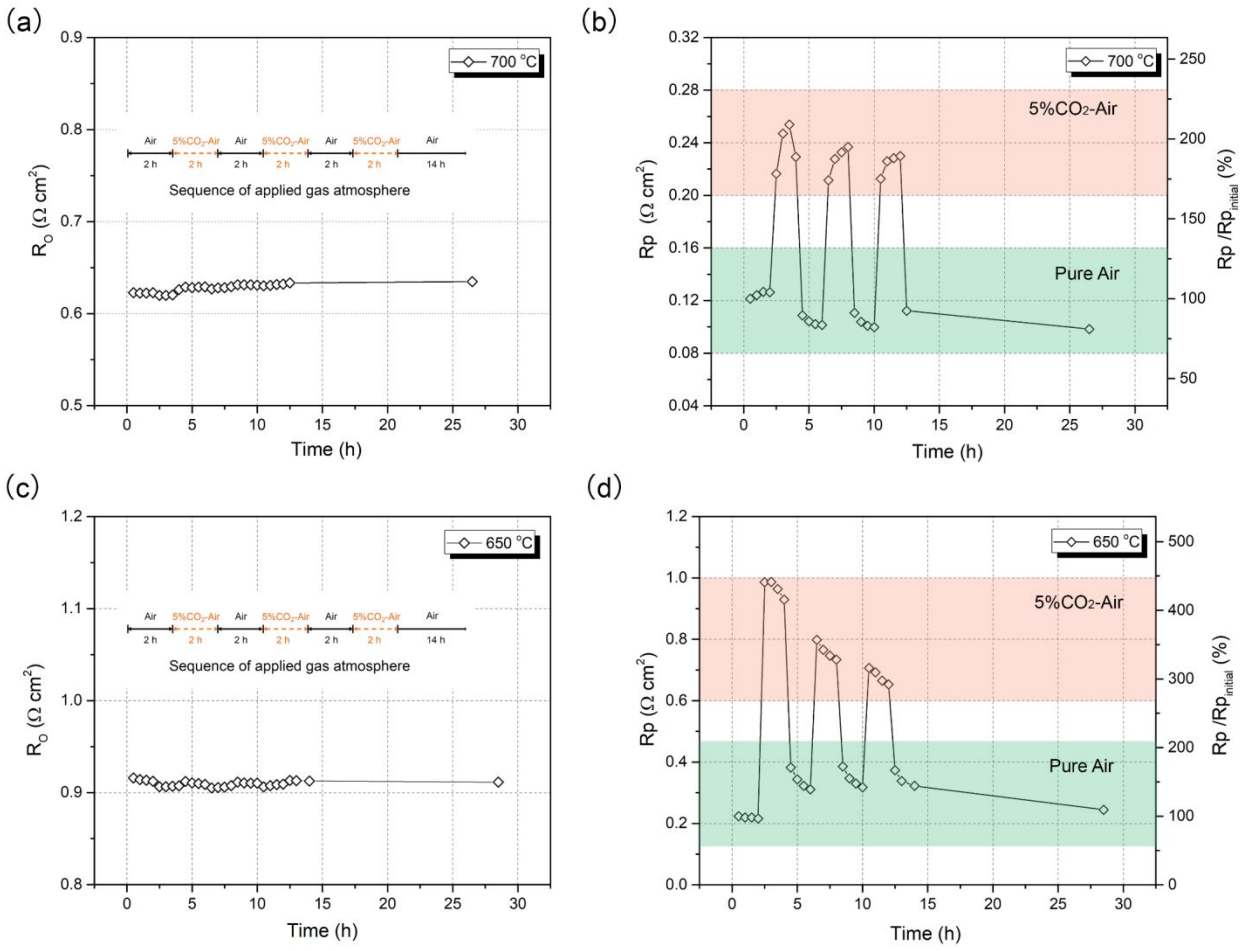
(a)
700 °C
Air 2 h
5%CO2-Air 2 h
Air 2 h
5%CO2-Air 2 h
Air 2 h
5%CO2-Air 2 h
Air 14 h
Sequence of applied gas atmosphere
R_O (Ω cm²)
Time (h)
(b)
700 °C
5%CO2-Air
Pure Air
Rp (Ω cm²)
Rp /Rp_initial (%)
Time (h)
(c)
650 °C
Sequence of applied gas atmosphere
R_O (Ω cm²)
Time (h)
(d)
650 °C
5%CO2-Air
Pure Air
Rp (Ω cm²)
Rp /Rp_initial (%)
Time (h)